Calculation of MLC in-air outputs using a leaf-field output subtraction method

S Kimura* [1,2], A Iwasaki[1], K Sutoh[2], M Seino[1], F Komai[1], M Sasamori[1]
(1) Hirosaki University, Hirosaki, Aomori, JP
(2) Aomori City Hospital, Aomori, Aomori, JP

Purpose: It is very important for the convolution dose calculation method to obtain information about how the in-air output, Sc (or collimator scatter factor) changes inside and outside of the multileaf collimator (MLC) field. Introducing a leaf-field output subtraction method, we calculate the in-air output for an MLC system. The leaf-field output subtraction method is to subtract the reduced in-air output due to each MLC leaf from the in-air output due to the jaw-collimator field. **Methods:** We employed a two-Gaussian source model for the radiation sources of the x-ray target and flattening filter. For calculation of in-air outputs at MLC fields, we took into account the structure of the MLC. Further, we took into account the attenuation of the MLC using a set of x-ray spectra that was a function of off-axis distance. We redesigned the MLC structure using (1) a simple structure MLC model and (2) a fine structure MLC model. **Results:** The two-Gaussian source model was effective especially in the neighborhood of the radiation field. The simple and fine structure MLC models could reflect the complex x-ray leakages from the rounded leaf end and tongue-groove of the actual MLC. For typical MLC fields, we calculated sets of in-air output distributions.

NOTES:

Introduction

In order to give a precise prescription dose in radiation therapy, we should use an accurate radiation therapy planning system. The convolution (or superposition) method [1-6] has been developed as a high-precision dose calculation algorithm. The technique spatially convolves the primary x-ray intensity with the dose kernel in media that describes the transport and energy deposition by secondary particles. The primary x-ray intensity can be evaluated using the in-air output along each rayline emanating from the source for a given radiation field..

Ahnesjö *et al* [7] have reported a method for calculating in-air outputs for MLC-shaped fields using a convolution model. Recently, the in-air output has been evaluated using single-Gaussian-source models [8, 9], two-Gaussian-source models [10], or three-Gaussian-source models [11]. In this paper, we propose to use a new type of two-Gaussian-source model for calculation of in-air outputs. One component is used for calculation of in-air outputs from the x-ray target (including the primary collimator) and the other for calculation of in-air outputs from the flattening filter. This two-Gaussian-source model is effective for calculation of in-air outputs for any field, including fields around the zero-area field. At the MLC-field beam irradiation, the complex structure of each MLC leaf with a partially curved end and a tongue-groove design should, in general, be taken into account [12]. For calculation of in-air outputs for MLC fields, we introduce a *leaf-field output subtraction method.* This method is to subtract the reduced in-air output due to each MLC leaf from the in-air output due to the jaw-collimator field. The method is effective for evaluation of the in-air output variation due to the leaf and interleaf transmission depending on the MLC leaf construction.

Theory

1. For jaw-collimator fields

As in Figure 1, we calculate the in-air outputs at the isocenter (P) using jaw-collimator fields, where we set three planes (the target, flattening filter, and isocenter planes). As x-ray output sources, we take the x-ray target and the flattening filter. Let the large-field in-air output from the x-ray target be unity, and let the large-field in-air output from the flattening filter be a_2. For a jaw-collimator field size (A_{jaw}) measured at the isocenter plane, the in-air output at point P from the x-ray target can be calculated [8-10] as

$$G_T(A_{jaw}) = \frac{1}{\pi(\lambda_T/2)^2}\int_{S_T} \exp[-R_T^2/(\lambda_T/2)^2]dS_T, \qquad (1)$$

where S_T is the rectangular area on the target plane, projected back from point P via the jaw collimator, R_T is the distance between the origin O_T (at the x-ray target point) and the area element (dS_T); $\lambda_T/2$ is the effective radius of the extended source of photons, measured on the x-ray target plane. Similarly, the in-air output from the flattening filter can be calculated using

$$G_F(A_{jaw}) = \frac{a_2}{\pi(\lambda_F/2)^2}\int_{S_F} \exp[-R_F^2/(\lambda_F/2)^2]dS_F, \qquad (2)$$

where S_F is the rectangular area on the flattening filter plane, projected back from point P via the jaw collimator, R_F is the distance between the origin O_F (at the middle of the flattening filter) and the area element (dS_F); $\lambda_F/2$ is the effective radius of the extended source of photons, measured on the flattening filter plane. Put

$$H(A_{jaw}) = (1 + a_1 \cdot C_{jaw}^{eq}) \times [G_T(A_{jaw}) + G_F(A_{jaw})], \qquad (3)$$

where C_{jaw}^{eq} is the side of the equivalent square field for the jaw-collimator field (A_{jaw}) and a_1 is the monitor-backscatter coefficient. Then $H(A_{jaw})$ expresses the total in-air output for a certain amount of the monitor unit (MU). Using a reference field of A_{jaw}=10×10 cm^2, the in-air output factor (S_c) for the jaw-collimator field (A_{jaw}) can be described as

$$S_c(A_{jaw}) = H(A_{jaw})/H(A_{jaw}=10\times10). \qquad (4)$$

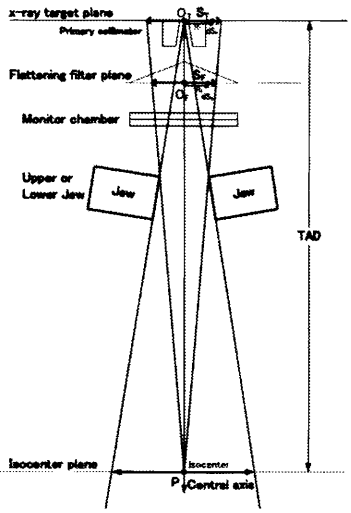

Figure 1. Diagram showing the geometry for S_c calculation at the isocenter (P). Points O_T and O_F are the origins on the x-ray target plane and flattening filter plane, respectively. S_T and S_F are the visible areas from point P via the jaw collimator, measured on the x-ray target plane and the flattening filter plane, respectively. R_T is the distance between the origin O_T and the area element (dS_T). R_F is the distance between the origin O_F and the area element (dS_F). *TAD* is the distance between the x-ray target and the isocenter.

2. For MLC Fields (the leaf-field output subtraction method)

For calculation of in-air outputs for MLC fields (Figure 2(a)), we use a simple or fine structure MLC model for the actual MLC (Figure 2(b)). Each MLC leaf is reconstructed using a thin MLC plate; however, performing the same x-ray attenuation along each rayline as the real MLC leaf does. In order to take into account in-air output increases due to the x-ray transmission through the MLC leaves, we propose a *leaf-field output subtraction method*. Moreover, in order to take into account the variation of the in-air output within and outside a jaw-collimator field, we introduce a source OCR (OCR_{source}) function, which expresses the relative in-air water collision kerma as a function of off-axis distance (R) for an imaginary infinite jaw-collimator field, letting $OCR_{source}(0)=1$ at the isocenter ($R=0$) (showing the in-air output variation caused by the design of the flattening filter). The details on the OCR_{source} function will be published elsewhere.

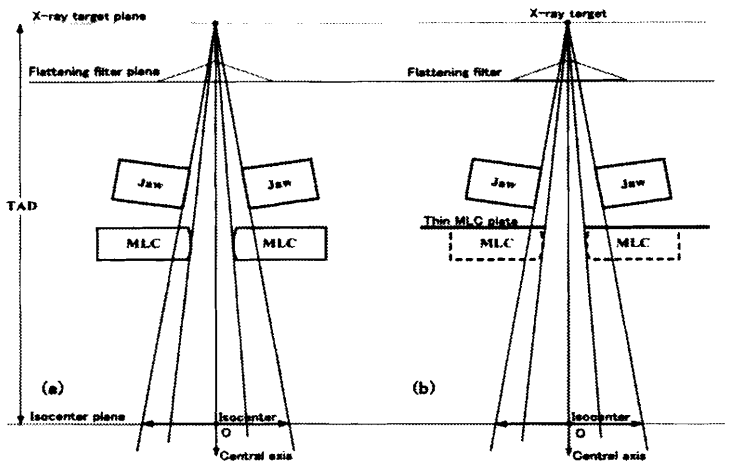

Figure 2. Diagrams showing the geometry of (a) the real MLC structure and (b) a simple or fine structure MLC model (thin MLC leaf plates are put at the top of the real MLC).

We calculate the in-air output at an arbitrary point P on the isocenter plane using an MLC field with a jaw-collimator field (A_{jaw}), as follows:

(1) Using the simple structure MLC model

This model enables us to calculate at high speed, remodelling each MLC leaf into a simple structure having a constant thickness. The rounded leaf end and the tongue-groove sides are redesigned to have simple cuts, letting its thin MLC plate perform the same x-ray attenuation along each rayline as the simple structure MLC does. On referring to Figure 3, the in-air output (S_c) factor at point P for an MLC field with a jaw-collimator field (A_{jaw}) can be calculated as

$$S_c(MLC)=[H(A_{jaw})-H_{MLC}]\cdot \mathrm{OCR}_{source}(R)/H(A_{jaw}=10\times10)_{isocenter}, \quad (5)$$

with

$$H_{MLC}=(1+a_1\cdot C_{jaw}^{eq})\times\sum_{leaf}(1-T_{leaf})[G_T(A_{leaf})+G_F(A_{leaf})], \quad (6)$$

$$G_T(A_{leaf})=\frac{1}{\pi(\lambda_T/2)^2}\int_{S'_T}\exp[-R_T^2/(\lambda_T/2)^2]dS'_T, \quad (7)$$

$$G_F(A_{leaf})=\frac{a_2}{\pi(\lambda_F/2)^2}\int_{S'_F}\exp[-R_F^2/(\lambda_F/2)^2]dS'_F, \quad (8)$$

where S'_T is the common rectangular area on the x-ray target plane, projected back from point P via the jaw collimator and via the thin MLC plate; S'_F be the common rectangular area on the flattening filter plane, projected back from point P via the jaw collimator and via the thin MLC-leaf plate; O_T is the x-ray target point; R_T is the distance between O_T and the area element (dS'_T); O_F is the intersection of the flattening filter plane and line P-O_T; R_F is the distance between O_F and the area element (dS'_F); R is the off-center distance for point P, measured on the isocenter plane; $H(A_{jaw}=10\times10)_{isocenter}$ is the in-air output (Equation (3)) at the isocenter ($R=0$) for a reference open jaw-collimator field of $A_{jaw}=10\times10$ cm^2 ($OCR_{source}(0)=1$ at the isocenter); and T_{leaf} is the x-ray transmission factor for the rayline (T) passing through the middle point of the common rectangular area on the thin MLC-leaf plate with respect to S'_T or S'_F ($T_{leaf}\leq1$) (note that the rayline (T) may be inside or outside the jaw-collimator field). It should be noted that when $T_{leaf}=1$, the MLC-leaf virtually does not exist in the jaw-collimator field.

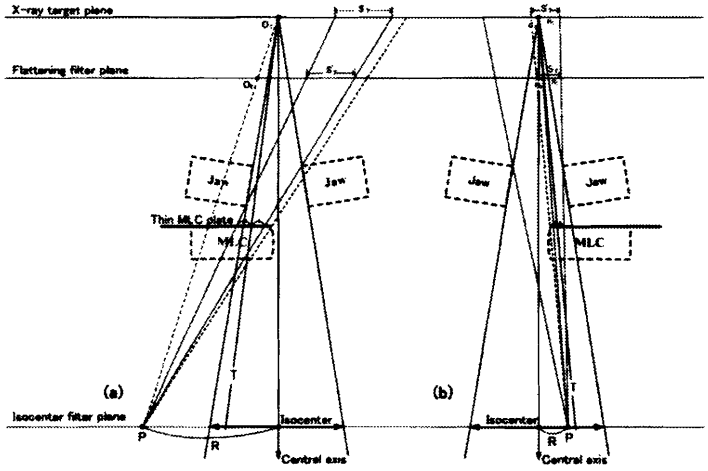

Figure 3. Diagrams showing cases where point P exists (a) outside and (b) inside the jaw-collimator field. The line (T) is the rayline that passes the middle point of the common rectangular area on the thin MLC plate.

(2) Using the fine structure MLC model

Using this model, we can take into account detailed x-ray leakages from many small sections of each MLC-leaf. As illustrated in Figure 4, each pair of MLC leaves (L=1-L_0) is divided into sections of a matrix (N,M) (N=1-N_0, M=1-M_0) according to the MLC structure. Let $\Delta A_{leaf}(N,M,L)$ denote showing the small rectangular area (on the isocenter plane) for a section (N,M) of a pair of thin MLC-leaf plates (L). Then the in-air output factor can be calculated as

$$S_c(MLC) = [H(A_{jaw}) - H_{MLC}] \cdot \mathrm{OCR}_{source}(R) / H(A_{jaw} = 10\times 10)_{isocenter}, \quad (9)$$

with

$$H_{MLC} = (1 + a_1 \cdot C_{jaw}^{eq}) \times \sum_{L=1}^{L_0} \sum_{M=1}^{M_0} \sum_{N=1}^{2N_0} [1 - T_{leaf}(N,M,L)] \{G_T(\Delta A_{leaf}(N,M,L)) + G_F(\Delta A_{leaf}(N,M,L))\}, \quad (10)$$

$$G_T(\Delta A_{leaf}(N,M,L)) = \frac{1}{\pi(\lambda_T/2)^2} \int_{S'_T} \exp[-R_T^2/(\lambda_T/2)^2] dS'_T, \quad (11)$$

$$G_F(\Delta A_{leaf}(N,M,L)) = \frac{a_2}{\pi(\lambda_F/2)^2} \int_{S'_F} \exp[-R_F^2/(\lambda_F/2)^2] dS'_F, \quad (12)$$

where S'_T be the common rectangular field on the x-ray target plane, projected back from point P via the jaw collimator and via the thin MLC-leaf for $\Delta A_{leaf}(N,M,L)$; S'_F be the common rectangular area on the flattening filter plane, projected back from point P via the jaw collimator and via the thin MLC-leaf plate for $\Delta A_{leaf}(N,M,L)$; R_T is the distance between the x-ray target point (O_T) and the area element (dS'_T); R_F is the distance between the rayline-dependent point (O_F) and the area element (dS'_F); R is the off-center distance for point P, measured on the isocenter plane; and $T_{leaf}(N,M,L)$ is the x-ray transmission factor for the rayline passing through the middle point of the common rectangular area projected back on the thin MLC-leaf plate with respect to S'_T or S'_F ($T_{leaf} \leq 1$) (note that the rayline may be inside or outside the jaw-collimator field).

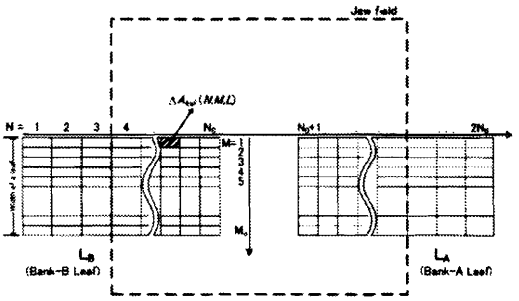

Figure 4. Diagram showing how the matrix (N,M,L) is taken using the fine structure MLC model.

Methods and results

The experimental study was conducted using 4 and 10 MV x-ray beams from a linear accelerator (Varian, CL-2100C, Mark II StandardMLC-80). The in-air measurement for jaw-collimator $S_c(A_{jaw})$ data was performed for square fields at the isocenter using a 0.6-cm^3 Farmer type ionization chamber, whose axis was arranged in parallel with the central axis. The ionization chamber was inserted into a polystyrene mini-phantom (4 cmϕ) or brass buildup caps. When using the mini-phantom, the ionization chamber was placed at a depth of 10 g/cm^2. The thicknesses of the brass buildup caps were 1.0 g/cm^2 for 4 MV x-rays and 2.5 g/cm^2 for 10 MV x-rays. Figure 5 shows two sets of S_c data for (a) 4 MV x-rays and (b) 10 MV x-rays, measured and calculated (Equation (4)) at the isocenter, where the calculations were performed using λ_T=0.2857 cm, λ_F=2.533 cm, a_1=0.0015 cm^{-1}, and a_2=0.0608 for 4 MV x-rays, and λ_T=0.2995 cm, λ_F=3.097 cm, a_1=0.0015 cm^{-1}, and a_2=0.083 for 10 MV x-rays; these sets of values were derived based on the measured sets of S_c data. Regarding the 4 MV x-ray beams, the minimum and maximum deviations of the calculated values are –0.18% to +0.17% for A_{jaw}=1.5×1.5 to 40×40 cm^2, –0.33% to +0.27% for A_{jaw}=1×1 to 40×40 cm^2. Regarding the 10 MV x-ray beams, the minimum and maximum deviations of the calculated values are –0.14% to +0.13% for A_{jaw}=1.9×1.9 to 40×40 cm^2, –0.14% to +0.13% for A_{jaw}=1.3×1.3 to 40×40 cm^2. It can be understood that for each of the 4 and 10 MV x-ray beams, the calculated S_c values agree well with the measured one and that both 4 and 10 MV x-ray S_c curves coincide well with each other.

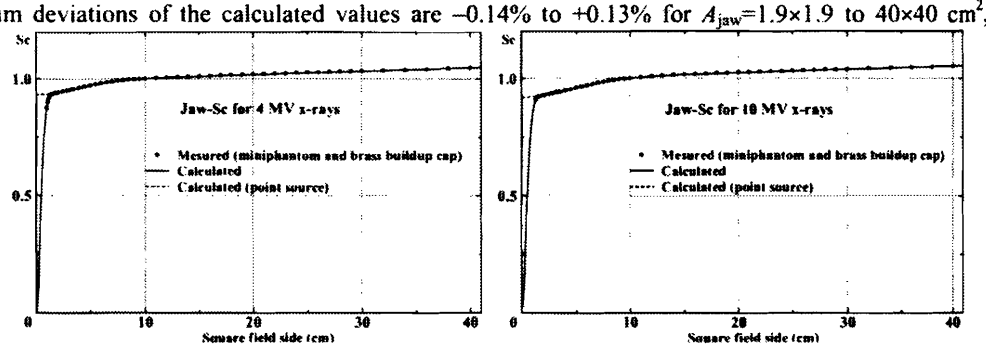

Figure 5. Sets of S_c data at isocenter for jaw square fields for (a) 4 MV x-rays and (b) 10 MV x-rays. The dotted marks were measured. The solid line was calculated assuming the x-ray target was an obscured source and the broken line assuming the x-ray target was a point source.

The broken lines in Figure 5 are calculated using λ_T=0 cm (the x-ray target source is assumed to be a perfect point source), showing very different data from the measured ones at small fields. Therefore, it can be understood that for points around field borders, the in-air output calculation should not carried out using λ_T=0 cm. It should be noted that sets of $S_c(A_{jaw})$ data measured at different off-axis distances are almost the same with each other; this means that the above-described integrations can be performed at any off-axis distance using a certain set of values for λ_T, λ_F, a_1, and a_2.

For calculation of T_{leaf} values (attenuation of the MLC leaf), we used sets of x-ray spectra as a function of off-axis distance (not shown in this paper). For an MLC irregular field with a jaw-collimator field of A_{jaw}=9×9 cm^2 (Figure 6), using the simple structure MLC model, we calculated how the in-air output factor (S_c) changes along lines (a) and (b) on the isocenter plane (Figure 7). Also for an MLC irregular field with a jaw-collimator field of A_{jaw}=12×12 cm^2, we calculated a two dimensional S_c distribution using the fine structure MLC model (Figure 8). However, the results are not illustrated in this paper.

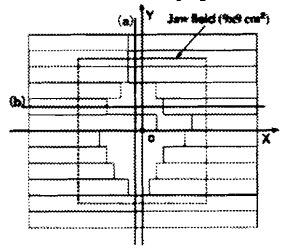

Figure 6. Geometry of an MLC irregular field with a jaw field of A_{jaw}=9×9 cm^2. MLC-S_c calculations were performed along lines (a) and (b).

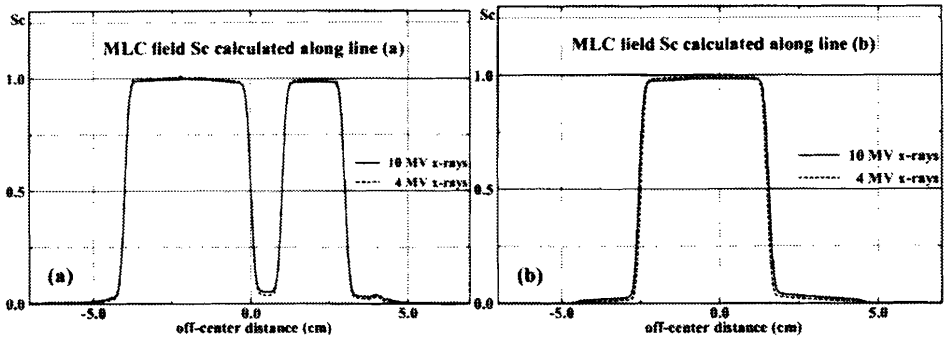

Figure 7. Two sets of MLC-S_c data calculated along (a) line (a) and (b) line (b) in Figure 6.

The in-air output distribution has very fine variations and they are very difficult to be measured accurately, so that whether these types of in-air output distributions are reasonable should be checked using in-phantom dose assessment. The *leaf-field output subtraction method* may improve the accuracy of convolution dose calculation especially for IMRT (intensity modulated radiation therapy).

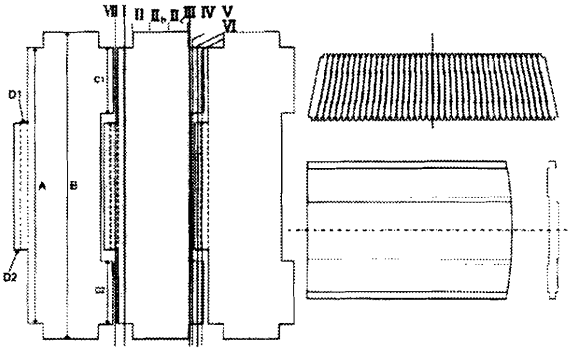

Figure 8. Diagrams showing an MLC structure with the rounded leaf end and tongue-groove views. For calculation of the x-ray transmission for each leaf, seven sections of I-VII were taken in the leaf width direction. The II section was further divided into 3 subsections (a-c). Therefore, the final sections were I(A), IIa(B), IIb(B), IIc(B), III(A), IV(C1+C2), V(C1+D2+C2), VI(C1+D1+C2), and VII(D1).

Conclusions

For calculation of in-air outputs, we proposed a two-Gaussian source model for the radiation sources of the x-ray target and flattening filter. For calculation of in-air outputs for MLC fields, we further proposed a *leaf-field output subtraction method*, redesigning the MLC structure using (1) a simple structure MLC model and (2) a fine structure MLC model, by which the complex x-ray leakages from the rounded leaf end and tongue-groove sides of the actual MLC leaf could be taken into account. It has been found that the two-Gaussian source model was effective especially in the neighborhood of the radiation field border.

References

[1] Boyer AL and Mok EC: A photon dose distribution model employing convolution calculations. Med. Phys. **12**, 169-177, 1985.

[2] Mackie TR, Scrimger JW, and Battista JJ: A convolution method of calculating dose for 15-MV x rays. Med. Phys. **12**, 188-196, 1985.

[3] Mohan R, Chui C, and Lidofsky L: Differential pencil beam dose computation model for photons. Med. Phys. **13**, 64-73, 1986.

[4] Ahnesjo A: Collapsed cone convolution of radiant energy for photon dose calculation in heterogeneous media. Med. Phys. **16**, 577-592, 1989.

[5] Iwasaki A: A convolution method for calculating 10-MV x-ray primary and scatter dose including electron contamination dose. Med. Phys. **19**, 907-915, 1992.

[6] Iwasaki A: 10 MV X-ray isocenter-axis dose calculation in thorax-like phantoms (water/cork) using the differential primary and scatter method. Radiat. Phys. Chem. **65**, 11-26, 2002.

[7] Ahnesjö A, Knöös T, Montelius A: Application of the convolution method for calculation of output factors for therapy photon beams. Med Phys, **19**: 295-301, 1992.

[8] Zhu TC and Bjärngard BE: The fraction of photons undergoing head scatter in x-ray beams. Phys. Med. Biol. **40**, 1127–1134, 1995.

[9] Zhu TC, Bjärngard BE, Xiao Y, *et al*: Modeling the output ratio in air for megavoltage photon beams. Med. Phys. **28**: 925-937, 2001.

[10] Zhu TC, Bjärngard BE: Head scatter off-axis for megavoltage x rays. Med Phys, **30**: 533–543, 2003.

[11] Jiang SB, Boyer AL and Ma C-MC: Modeling the extrafocal radiation and monitor chamber backscatter for photon beam dose calculation. Med. Phys. **28**: 55-66, 2001.

[12] AAPM Report No. 72: Basic applications of multileaf collimators. AAPM, 2001.

Introduction of an off-axis collimator scatter factor (SC) and a source off-center ratio (OCRsource) for calculation of off-axis in-air outputs

F Komai*, A Iwasaki, S Kimura, M Seino, M Sasamori
Hirosaki University, Hirosaki, Aomori, JP

Purpose: When using convolution methods, it is important to obtain an in-air output distribution for a given open jaw-collimator field. We propose a method for calculating the off-axis in-air output. The flattening filter is so designed that the in-air output may increase with the off-axis distance. **Methods and results:** We introduce an off-axis collimator scatter factor (S_C) and a source off-center ratio (OCR_{source}) for calculating off-axis in-air outputs. The off-axis S_C factor is remade using the jaw-collimator factor (H_{jaw}) proposed by Zhu and Bjärngard, expressing the in-air output variation caused by setting the jaw collimators in an infinite field. The OCR_{source} expresses the in-air output variation with the off-axis distance at an infinite jaw-collimator field. We calculate the in-air output as a product of the off-axis S_C factor and the OCR_{source}. The study was carried out using open jaw-collimator fields of a linear accelerator producing 4 and 10 MV x-rays. For evaluation of the H_{jaw} factor we took the x-ray target as a small obscure radiation source and the flattening filter as a large obscure radiation source. It was assumed that each of the radiation sources had a Gaussian lateral spread. The H_{jaw} factor expression was rebuilt based on S_C factor data measured at isocenter. The OCR_{source} was evaluated by taking into account both the off-axis S_C factor and the off-axis spectral change for in-air dose data measured along a transversal line across a jaw-collimator field using an ionization chamber with an acrylic buildup cap. It has been found that the OCR_{source} increases with the off-axis distance, showing the off-axis in-air output variation caused by the design of the flattening filter and that taking into account the off-axis spectral change for deriving OCR_{source} data is effective when using buildup caps of high Z materials.

NOTES:

Introduction

In order to calculate the dose at a point in a medium irradiated by high-energy photons, the convolution method utilizes the primary photon beam intensity in the medium as a parameter along each rayline emanating from the source. It is fundamental to obtain in-air output data on a plane for a given open field formed by the jaw collimator system. For calculation of the off-axis in-air output, we propose to use an off-axis collimator scatter factor (S_C) and a source off-center ratio (OCR_{source}). The off-axis S_C factor is remade using the jaw-collimator factor (H_{jaw}) proposed by by Zhu and Bjärngard [1], expressing the in-air output variation caused by setting the jaw collimators in an infinite field. This time, the H_{jaw} factor is evaluated using a Gaussian source model for each of the flattening filter and the x-ray target. The OCR_{source} expresses the in-air output variation with the off-axis distance in an infinite jaw-collimator field, showing the off-axis in-air output variation caused by the design of the flattening filter. We calculate the off-axis in-air output as a product of the off-axis S_C factor and the OCR_{source}.

Theory

The theoretical study is carried out using open jaw-collimator fields that are rectangular in shape. As in figure 1, we calculate the in-air output (OP) at an arbitrary point (X_0,Y_0) on the isocenter plane for a given jaw-collimator field (A_0) measured at the isocenter. The origin O of the orthogonal X_0 and Y_0 coordinates is set at the isocenter. Then the off-axis distance for point (X_0,Y_0) is $R_0=(X_0^2+Y_0^2)^{1/2}$ on the isocenter plane.

The OCR_{source} is defined as the ratio of the in-air output at point (X_0,Y_0) to that at the origin O using an imaginary infinite jaw-collimator field. We can usually take it symmetrical with respect to the central axis. In this paper, we put it as a function of off-axis distance (R_0); namely, $OCR_{source}(0)=1$ for $R_0=0$. The H_{jaw} factor is reconstructed using the concept of Zhu and Bjärngard [1]. It expresses the in-air output variation caused by setting the jaw collimator in an infinite field. We take the x-ray target (including the primary collimator) as a small obscure radiation source and the flattening filter as a large obscure radiation source, assuming that each of the radiation sources has a Gaussian lateral spread. First, without taking into account the effect of the monitor-backscatter from the jaw collimator for the monitor unit (MU), we calculate the in-air output at the center of a large jaw-collimator field as unity from the x-ray target and as a_2 from the flattening filter. Second, using the off-axis S_C factor defined as a ratio of two H_{jaw} factors with a monitor-backscatter coefficient (a_1) and using the OCR_{source}, we calculate the in-air output (OP) at point (X_0,Y_0) as follows:

$$OP(X_0,Y_0;A_0)=S_C(X_0,Y_0;A_0)\times OCR_{source}(R_0), \tag{1}$$

where

$$S_C(X_0,Y_0;A_0)=H_{jaw}(X_0,Y_0;A_0)/H_{jaw}(X_0,Y_0;10\times10), \tag{2}$$

with

$$H_{jaw}(X_0,Y_0;A_0)=(1+a_1\cdot C_0^{eq})\times[1\cdot G_T(X_0,Y_0)+a_2\cdot G_F(X_0,Y_0)], \tag{3}$$

$$G_T(X_0,Y_0)=\frac{1}{\pi(\lambda_T/2)^2}\int_{S_T}\exp[-R_T^2/(\lambda_T/2)^2]dS_T. \tag{4}$$

$$G_F(X_0,Y_0)=\frac{1}{\pi(\lambda_F/2)^2}\int_{S_F}\exp[-R_F^2/(\lambda_F/2)^2]dS_F. \tag{5}$$

The area (S_T) is taken at the x-ray target plane, and the area (S_F) at the flattening filter plane that is situated at the bottom of the flattening filter. R_T is the distance between the origin O_T and the area element (dS_T), and $\lambda_T/2$ is the effective radius of the x-ray target. R_F is the distance between the origin O_F and the area element (dS_F), and $\lambda_F/2$ is the effective radius of the extended source of photons on the flattening filter plane. In Eq. (3), the monitor-backscatter factor $(1+a_1\cdot C_0^{eq})$ is calculated using the side (C_0^{eq}) of the equivalent square field for the jaw-collimator field (A_0). Note that the H_{jaw} factor of Eq. (3) becomes infinite for $C_0^{eq}=\infty$ and zero for $C_0^{eq}=0$; therefore, the off-axis S_C factor cannot be normalized at an infinite field nor at zero field. Accordingly, the off-axis S_C factor is normalized using a reference field of 10×10 cm^2, setting the center of the reference field at point (X_0,Y_0). It can be seen that the in-air output (OP) at the isocenter for $A_0=10\times10$ cm^2 is calculated as unity. The off-axis S_C factor can also be defined as

$$S_C(X_0,Y_0;A_0)=OP(X_0,Y_0;A_0)/OP(X_0,Y_0;10\times10). \tag{6}$$

It can be seen from Eqs. (3)-(5) that the off-axis S_C factor should not depend on the measuring point (X_0,Y_0) and that the constants of λ_T, λ_F, a_1, and a_2 can be determined based on measurable off-axis S_C data at any point (X_0,Y_0).

For evaluation of OCR_{source} data by measurement, we take a case in which a typical ionization chamber with a buildup cap is irradiated in free air. Then it can be understood that the in-air chamber reading (K_{cap}) virtually reflects the in-air collision kerma defined using the buildup cap material. Here both points (X_0,Y_0) and (0,0) should be inside a jaw-collimator field (A_0) and the center of the jaw-collimator field (A_0) should coincide with point (0,0). We introduce a factor of OCR_{cap} for point (X_0,Y_0), which is defined as

$$OCR_{cap}(X_0,Y_0;A_0) = K_{cap}(X_0,Y_0;A_0)/K_{cap}(0,0;A_0). \tag{7}$$

It should be noted that the OCR_{cap} is measurable. We also introduce a factor of OCR_{water} for point (X_0,Y_0) that is evaluated using the water collision kerma (K_{water}), which is defined as

$$OCR_{water}(X_0,Y_0;A_0) = K_{water}(X_0,Y_0;A_0)/K_{water}(0,0;A_0). \tag{8}$$

By taking into account the off-axis spectral difference at points (X_0,Y_0) and (0,0) for the OCR_{cap} and OCR_{water} functions, the relationship between the two OCR factors becomes

$$OCR_{water}(X_0,Y_0;A_0) = OCR_{cap}(X_0,Y_0;A_0)\times\frac{\sum_{i=1}^{i_{max}}\Psi_0(0;E_i)\Delta E_i[\mu_{en}(E_i)/\rho]_{cap}}{\sum_{i=1}^{i_{max}}\Psi_0(R_0;E_i)\Delta E_i[\mu_{en}(E_i)/\rho]_{cap}}\times\frac{\sum_{i=1}^{i_{max}}\Psi_0(R_0;E_i)\Delta E_i[\mu_{en}(E_i)/\rho]_{water}}{\sum_{i=1}^{i_{max}}\Psi_0(0;E_i)\Delta E_i[\mu_{en}(E_i)/\rho]_{water}}, \tag{9}$$

where $\Psi_0(R_0;E_i)$ expresses the energy fluence for photon energy E_i and energy bin width ΔE_i ($i=1-i_{max}$) at an off-axis distance of $R_0=(X_0^2+Y_0^2)^{1/2}$. Note that the OCR_{water} function is derived without taking into account the photon attenuation within the buildup cap. Using the H_{jaw} factor, the OCR_{water} for an imaginary infinite field can be calculated as

$$OCR_{water}(X_0,Y_0;\infty) = OCR_{water}(X_0,Y_0;A_0)\times\frac{H_{jaw}(0,0;A_0)}{H_{jaw}(X_0,Y_0;A_0)}. \tag{10}$$

We put $OCR_{source}(R_0)=OCR_{water}(X_0,Y_0;\infty)$ using $R_0=(X_0^2+Y_0^2)^{1/2}$, then we have $OCR_{source}(0)=1$ for $R_0=0$.

Methods and results

The experimental study was conducted using a linear accelerator (Mitsubishi EXL-15DP) producing 4 and 10 MV x-rays. Sets of energy fluence spectra $[\Psi_0(R_0;E_i)]$ as a function of off-axis distance (R_0) were estimated using the Waggener-Iwasaki iterative perturbation method [2]. Figure 2 shows sets of (a) 4 MV and (b) 10 MV photon fluence spectra (Φ_0) using a relationship of $\Phi_0(R_0;E_i)=\Psi_0(R_0;E_i)\Delta E_i/E_i$, where we normalize the photon fluence spectrum (Φ_0) for each off-axis distance (R_0) as

$$\sum_{i=1}^{i_{max}}\Phi_0(R_0;E_i) = 1. \tag{11}$$

This is because such a normalized photon fluence spectrum (Φ_0) can be clearly emphasized as a function of off-axis distance (R_0). The fact has been obtained that the logarithm of the normalized photon fluence spectrum (Φ_0) at each energy bin is almost proportional to the off-axis distance (R_0).

For each of the x-ray beams, the S_C factor was measured at the isocenter ($X_0=Y_0=0$) using a lead buildup cap and acrylic mini-phantoms of 2 and 4 cmϕ. The lead buildup cap was useful for measuring S_C data at small fields. Figure 3 shows sets of S_C data for the (a) 4 MV and (b) 10 MV x-ray beams, where the plotted marks were measured. Two sets of λ_T, λ_F, a_1, and a_2 values were derived based on the plotted marks as λ_T=0.394 cm, λ_F=2.354 cm, a_1= 0.000910 cm^{-1}, and a_2 =0.0506 for the 4 MV x-ray beam and λ_T=0.368 cm, λ_F=3.335 cm, a_1=0.000573 cm^{-1}, and a_2 =0.0621 for the 10 MV x-ray beam. The solid lines in figure 3 were drawn using Eq. (2) with the corresponding sets of λ_T, λ_F, a_1, and a_2 values. As may be seen from figure 3, both S_C lines almost coincide with each other.

For measurement of OCR_{cap} data for each of the x-ray beams with a jaw-collimator field of A_0=40×40 cm^2, we used a typical thimble chamber with an acrylic buildup cap whose thickness was enough to avoid electron contamination for chamber readings. Figure 4 shows OCR_{cap} data using Eq. (7) (in dotted marks), OCR_{water} data using Eq. (10) (in white circles), and OCR_{source} data smoothed for an infinite field (in solid curves) as a function of off-axis distance (R_0) for the (a) 4 MV and (b) 10 MV x-ray beams. It can be seen that each of the OCR_{source} curves generally increases with the off-axis distance (R_0). It can also be seen that the differences between OCR_{cap} and OCR_{water} data are small except at large off-axis distances. This fact indicates that the difference between $[\mu_{en}(E_i)/\rho]_{cap}$ and $[\mu_{en}(E_i)/\rho]_{water}$ values for each energy bin in Eq. (9) is small when using acrylic buildup

caps. However, when using lead buildup caps, the differences between OCR_{cap} and OCR_{water} data are large (not shown in this paper). Therefore, it can be understood that taking into account the off-axis spectral change for deriving OCR_{source} data is effective when using buildup caps of high Z materials.

Conclusion

We have developed a method of calculating off-axis in-air outputs for open jaw-collimator fields using an off-axis collimator scatter factor (S_C) and a source off-center ratio (OCR_{source}). The off-axis S_C factor is remade using the jaw-collimator factor (H_{jaw}) proposed by Zhu and Bjärngard [1], expressing the in-air output variation caused by setting the jaw collimators in an infinite field. The OCR_{source} expresses the in-air output variation with the off-axis distance at an infinite jaw-collimator field. The study was carried out using open jaw-collimator fields of a linear accelerator. For evaluation of the H_{jaw} factor we took the x-ray target as a small obscure radiation source and the flattening filter as a large obscure radiation source. It was assumed that each of the radiation sources had a Gaussian lateral spread. The H_{jaw} factor expression was rebuilt based on S_C factor data measured at isocenter. The OCR_{source} was evaluated by taking into account both the S_C factor and the off-axis spectral change for in-air dose data measured along a transversal line across a jaw-collimator field using an ionization chamber with an acrylic buildup cap. The following results were obtained for 4 and 10 MV x-rays: (1) The OCR_{source} generally increases with the off-axis distance (showing the in-air output variation caused by the design of the flattening filter). (2) Taking into account the off-axis spectral change for deriving OCR_{source} data is effective when using buildup caps of high Z materials.

References

[1] Zhu TC and Bjärngard BE, "Head scatter off-axis for megavoltage x rays," *Med. Phys.* **30**, 533-543 (2003).

[2] Iwasaki A, Kubota M, Hirota J, Fujimori A, Suzaki K, Aoki M, and Abe Y, "Characteristic features of a high-energy x-ray spectra estimation method based on the Waggener iterative perturbation principle," *Med. Phys.* **33**, 4056-4063 (2006).

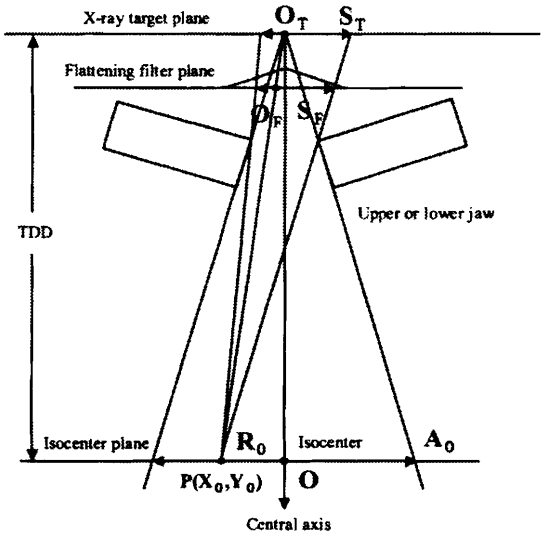

Figure 1. Diagram showing how to calculate the in-air output (OP) at an arbitrary point (X_0, Y_0) on the isocenter plane for a given jaw-collimator field (A_0) measured at isocenter.

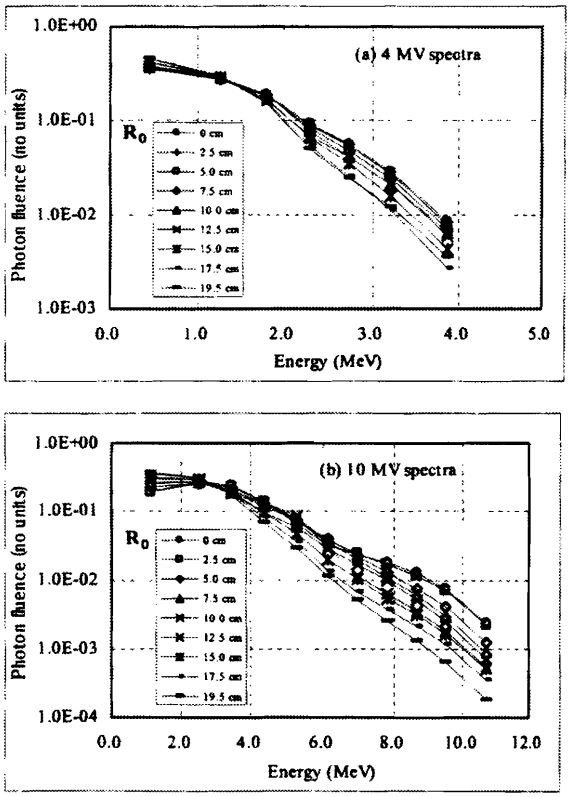

Figure 2. Sets of (a) 4 MV and (b) 10 MV photon fluence spectra (Φ_0) as a function of off-axis distance (R_0).

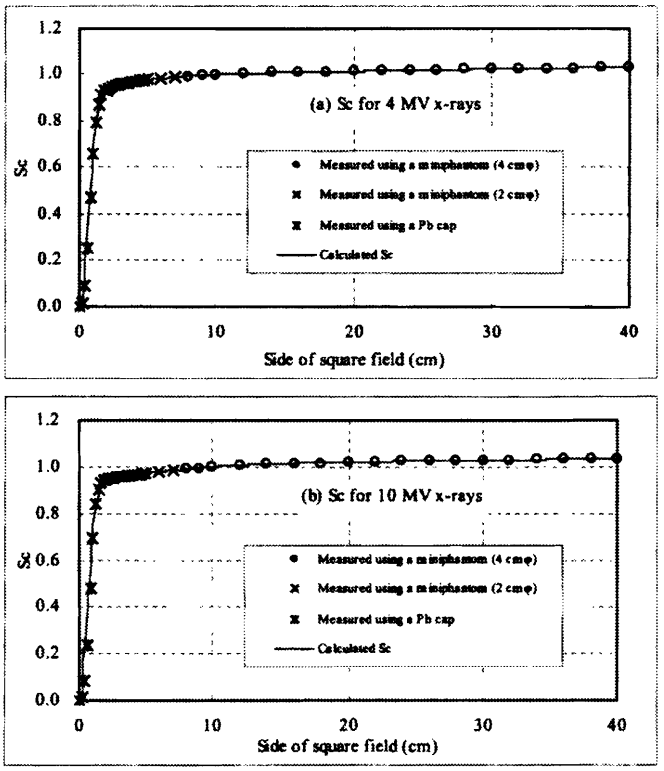

Figure 3. Sets of S_C data for (a) 4 MV and (b) 10 MV x-ray beams. Plotted marks were measured. Solid lines were drawn using Eq. (2) with the corresponding sets of λ_T, λ_F, a_1, and a_2 values.

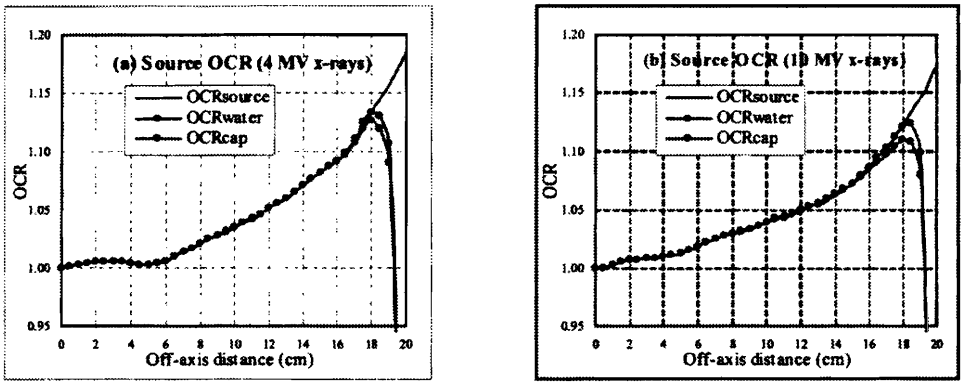

Figure 4. Sets of OCR_{cap} data using Eq. (7) (in dotted marks), OCR_{water} data using Eq. (10) (in white circles), and OCR_{source} data smoothed for an infinite field (in solid curves) as a function of off-axis distance (R_0) for (a) 4 MV and (b) 10 MV x-ray beams.

Proposals to improve the accuracy of convolution-based dose calculation

A Iwasaki*, S Kimura, M Seino, F Komai, M Sasamori
Hirosaki University, Hirosaki, Aomori, JP

The present convolution methods have two serious problems: One is that only one dose kernel constructed using a certain x-ray spectrum for a given accelerating voltage is employed; therefore, the dose kernel hardening effect along each rayline is raised. The other is that the incident x-ray spectrum as a function of off-axis is not verified by measurement for each linear accelerator; therefore, the primary beam intensity along each rayline may happen to be evaluated inaccurately. Iwasaki (2006) has developed a method for estimating high-energy x-ray spectra using only about ten energy bins. The method can estimate a set of spectra as a function of off-axis distance using a common set of energy bins. It has been found that the method can estimate spectra guaranteed for all Z materials usually used in high-energy x-ray radiotherapy. In order to improve the accuracy of dose calculation due to the convolution methods, we propose algorithms (a) to use a set of spectra as a function of off-axis distance using a common set of only about ten energy bins, (b) to use of multiple dose kernels constructed for a common set of energy bins, (c) to calculate the primary beam intensity for open jaw-collimator fields, and (d) to calculate the primary beam intensity for MLC fields, introducing a leaf-field output subtraction method.

NOTES:

Introduction

The convolution dose calculation method is one of the model-based approaches. It is convenient for 3-D calculations, especially when using irregular fields with a non-uniform incident beam intensity. The technique spatially convolves the primary x-ray intensity with the dose kernel in media that describes the transport and energy deposition by secondary particles. Dose kernels for materials different from water are usually reproduced from the in-water dose kernel using the density-scaling theorem [1].

Iwasaki [2,3] has reported a method for estimating x-ray spectra applicable for media at least from water to lead using only about ten energy bins (the computer soft is available at Synthetic Planning Industry Co., Ltd. at HK Bldg 3F, 2-21-10 Nishiogi-minami, Suginami-ku, Tokyo 167-0053, Japan; website: www.spi-sys.co.jp; e-mail address: info@spi-sys.co.jp). Using a common set of energy bins, the spectrum can be estimated as a function of off-axis distance. Therefore, using spectra of this kind, we can practically perform convolution-based dose calculations based on multiple pairs of dose kernel and primary beam intensity constructed for the energy bins. In this case, we do not need to take into account kernel hardening and beam hardening phenomena for dose calculations [4,5]. In order to improve the accuracy of convolution-based dose calculation, this paper proposes some important techniques regarding (a) use of spectra as a function of off-axis distance, (b) use of multiple dose kernels, (c) calculation of the primary beam intensity for open jaw-collimator fields, and (d) calculation of the primary beam intensity for MLC fields.

Proposals

A. Use of spectra as a function of off-axis distance

When using convolution dose calculation methods, information on the x-ray spectrum as a function of off-axis distance is very important for accurate dose calculations. This is because they calculate the dose on the basis of primary beam intensity data along each rayline. Especially when an x-ray beam penetrates through a wedge or compensator made of a high Z material like lead, both the spectrum and primary beam intensity variations are generally great.

The Waggener-Iwasaki iterative perturbation method [2,3] enables us to estimate sets of photon fluence spectra (Φ_0) as a function of off-axis distance (R_0) using a common set of only about ten representative photon energies. Figure 1 shows an example from a 10 MV x-ray linear accelerator, where the photon fluence spectrum (Φ_0) at each off-axis distance (R_0) is normalized as

$$\sum_{i=1}^{i_{max}} \Phi_0(R_0; E_i) = 1, \qquad (1)$$

where E_i is the representative photon energy of the ith energy bin. It has been found that the normalized photon fluence spectrum (Φ_0) can be clearly emphasized as a function of off-axis distance (R_0). The fact has been obtained that the logarithm of the normalized photon fluence spectrum (Φ_0) at each energy bin is almost proportional to the off-axis distance (R_0).

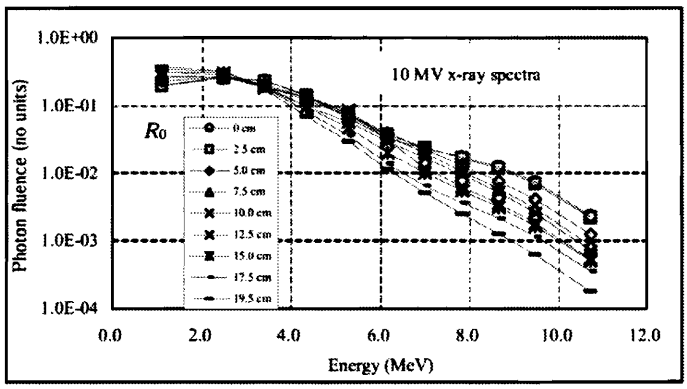

Figure 1. Sets of 10 MV photon fluence spectra (Φ_0) as a function of off-axis distance (R_0).

B. Use of multiple dose kernels

The in-water dose kernels used for convolution methods are usually produced using Monte Carlo simulation with the interaction point forced to the center of a large water phantom [6-9]. However, it is still not clear whether such Monte Carlo-based kernels

allow accurate dose calculations with a wide range of field sizes and depths, especially in thorax phantoms. Using the differential primary and scatter concept, Iwasaki [10-12] has proposed another type of in-water dose kernel, with which perfectly accurate primary and scatter dose can be recalculated under conditions that the beam is parallel, the incident beam intensity is uniform within and zero outside the field, and the primary beam attenuation coefficient along raylines is not a function of depth and off-axis distance. In a sense, this type of in-water dose kernel is a mosaic dose kernel because it is reconstructed using a set of semi-infinite water phantoms.

Figure 2 shows the geometry for obtaining a mosaic dose kernel: (a) $H_1(\xi,r;E_i)$ expresses the forward primary or scatter dose at a point (ξ,r), arising from the E_i photon pencil-beam interaction point O (ξ=0,r=0) situated on the phantom surface, per unit primary water collision kerma per unit volume at point O; and (b) $H_2(\eta,r;E_i)$ expresses the backward primary or scatter dose at a point (η,r) on the phantom surface, arising from the E_i photon pencil-beam interaction point O (η=0,r=0) situated at a depth η below the phantom surface, per unit primary water collision kerma per unit volume at point O. With respect to the $H_1(\xi,r;E_i)$ and $H_2(\eta,r;E_i)$ functions, we can obtain $H_1(0,r;E_i)=H_2(0,r;E_i)$ for $\xi\rightarrow 0$ and $\eta\rightarrow 0$. We should make dose kernels for a common set of energy bins of the x-ray spectrum.

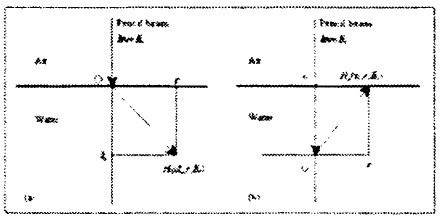

Figure 2. Diagrams showing how (a) the $H_1(\xi,r;E_i)$ function and (b) the $H_2(\eta,r;E_i)$ function should be used in water for a given E_i photon pencil-beam, where the interaction point is situated at point O.

The primary or scatter dose for each of the representative photon energies (E_i for i=1–i_{max}) is calculated using its primary intensity along each rayline and its primary or scatter dose kernel. On referring to figure 3 showing an irradiation for a homogeneous water phantom, the primary dose at point P from the volume elements (Δv) at points (ξ,r) and (η,r) for the whole energy bins (i=1-i_{max}) can be calculated as

$$D_{prim}=\sum_{i=1}^{i_{max}} H_{prim}(\xi,r;E_i)\cdot K_{col}(\xi,r;E_i)\cdot\Delta v+\sum_{i=1}^{i_{max}} H_{prim}(\eta,r;E_i)\cdot K_{col}(\eta,r;E_i)\cdot\Delta v. \quad (2)$$

Similarly, the scatter dose at point P can be calculated as

$$D_{scat}=\sum_{i=1}^{i_{max}} H_{scat}(\xi,r;E_i)\cdot K_{col}(\xi,r;E_i)\cdot\Delta v+\sum_{i=1}^{i_{max}} H_{scat}(\eta,r;E_i)\cdot K_{col}(\eta,r;E_i)\cdot\Delta v. \quad (3)$$

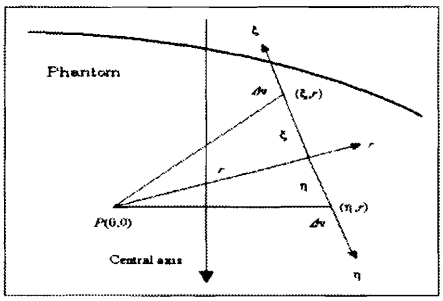

Figure 3. Diagram showing how the primary or scatter dose at point P from the volume elements (Δv) at points (ξ,r) and (η,r) can be calculated within a homogeneous water phantom.

The primary and scatter dose calculations are performed using the primary and scatter dose kernels [$H_{prim}(\xi,r;E_i)$, $H_{prim}(\eta,r;E_i)$, $H_{scat}(\xi,r;E_i)$, and $H_{scat}(\eta,r;E_i)$] applied to the primary water collision kerma [$K_{col}(\xi,r;E_i)$ and $K_{col}(\eta,r;E_i)$] for each of the representative photon energies (E_i) along each rayline.

We produced two kinds of in-water primary dose kernels (with voxel sizes of 0.5×0.5 mm^2) in water for 10 MeV photons using Monte Carlo simulation. As illustrated in figure 4, one was (a) an ordinary primary dose kernel with the interaction point forced to the center of a large water phantom (the dose kernel value at the voxel of the photon interaction point O is 87.6 cm^{-3}) and (b) a mosaic primary dose kernel (the dose kernel value at the voxel of the photon interaction point O is 42.5 cm^{-3}). It has been found that around the photon interaction point, the mosaic dose kernel takes much lower dose values than the ordinary dose kernel (the details are not clearly shown in the diagrams); however, at points far from the photon interaction point, the mosaic dose kernel and the ordinary dose kernel take almost the same dose values. This fact may lead to severe dose calculation differences depending on which dose kernel is used, especially for thorax irradiations with small fields. Actually, the fact has

been obtained that the mosaic dose kernel can generally perform more accurate dose calculations in water than the ordinary dose kernel when the field is very small (less than a radius of about 0.5 cm for 10 MeV photons).

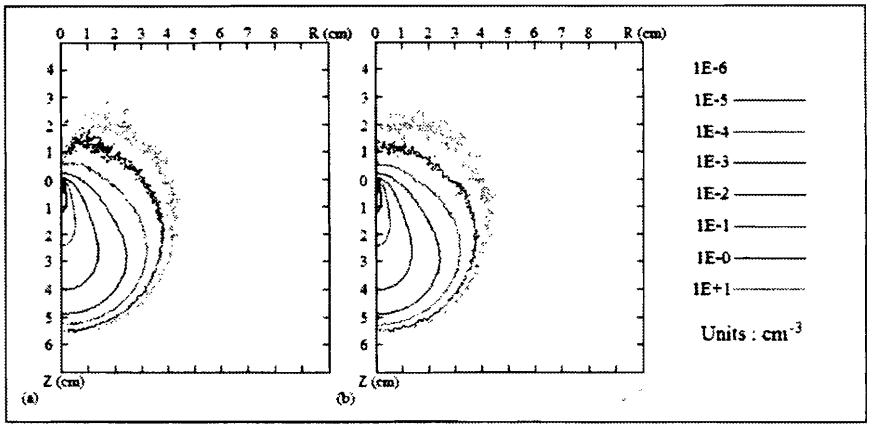

Figure 4. (a) An ordinary primary dose kernel and (b) a mosaic primary dose kernel for monochromatic 10 MeV photons, produced using Monte Carlo simulation.

C. Calculation of the primary beam intensity for open jaw-collimator fields

In order to calculate the dose at a point in a medium irradiated by x rays from a linear accelerator, the convolution method utilizes the primary beam intensity in the medium as a parameter along each rayline emanating from the source. Therefore, it is fundamental to obtain in-air output data on a plane for a given open rectangular field formed by the jaw collimator system. For calculation of the in-air output, we propose a method to use a jaw-collimator factor (H_{jaw}) and a source off-center ratio (OCR_{source}). The H_{jaw} factor expresses the in-air output variation caused by setting the jaw collimator in an infinite field, as proposed by Zhu and Bjärngard [13]. It is evaluated using a Gaussian source model for each of the flattening filter and the x-ray target, taking into account the monitor-backscatter effect for the monitor unit (MU). The OCR_{source} expresses the in-air output variation with the off-axis distance in an imaginary infinite jaw-collimator field, showing the in-air output variation caused by the design of the flattening filter. We finally calculate the in-air output as a product of the OCR_{source} and the off-axis collimator scatter factor (S_C) derived using H_{jaw} factors. Figure 5 shows an OCR_{source} curve for a 10 MV x-ray beam from a linear accelerator.

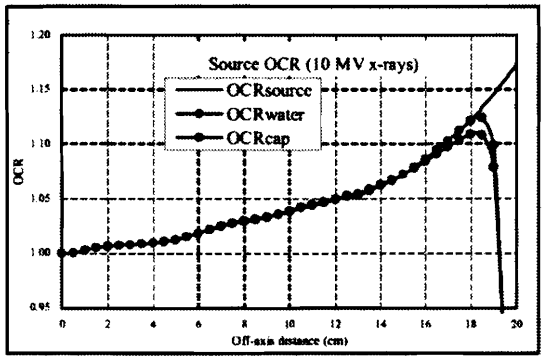

Figure 5. OCR_{source} data (in solid line) for an infinite field as a function of off-axis distance (R_0) for a 10 MV x-ray beam. Sets of OCR_{cap} data (in dotted marks) and OCR_{water} data (in white circles) used for deriving the OCR_{source} data are also illustrated.

D. Calculation of the primary beam intensity for MLC fields

In order to calculate the in-air output for multileaf collimator (MLC) fields, we introduce a *leaf-field output subtraction method*, in which the following calculation techniques are used:

(a) A two-Gaussian-source model is used for calculating the in-air output, taking the x-ray target and the flattening filter as output sources.
(b) Beam attenuation due to the MLC is calculated using x-ray spectra as a function of off-axis distance.
(c) The source off-center ratio (OCR_{source}) is introduced, showing the off-axis in-air output variation caused by the design of the flattening filter.

The basic constants in the two-Gaussian-source model can be derived based on collimator scatter factor (S_c) data measured at jaw-collimator fields. Figure 6 shows 4 and 10 MV x-ray in-air output distributions along line (a) across an MLC field at a jaw-collimator field of A_0=9×9 cm^2. The in-air output distribution has very fine variations and they are very difficult to be measured correctly, so that whether these types of in-air output distributions are reasonable should be checked using in-phantom dose assessment. The leaf-field output subtraction method may improve the accuracy of convolution dose calculation especially for IMRT (intensity modulated radiation therapy).

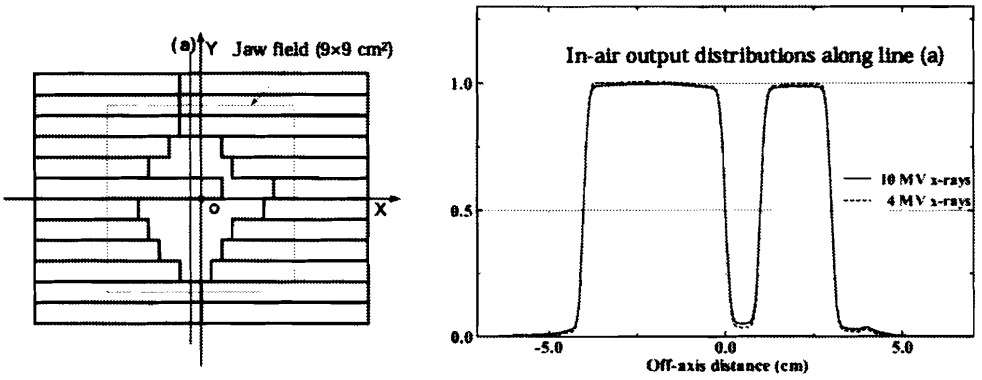

Figure 6. In-air output distributions along line (a) across an MLC field at a jaw-collimator field of A_0=9×9 cm^2 for 4 and 10 MV x-ray beams.

Summary

In order to improve the accuracy of convolution dose calculation, we proposed algorithms (a) to use a set of spectra as a function of off-axis distance using a common set of only about ten energy bins, (b) to use of multiple dose kernels constructed for a common set of energy bins, (c) to calculate the primary beam intensity for open jaw-collimator fields, and (d) to calculate the primary beam intensity for MLC fields, introducing a leaf-field output subtraction method.

References

[1] O'Connor JE, "The variation of scattered x-rays with density in an irradiated body," *Phys. Med. Biol.* **1**, 352-369 (1957).

[2] Iwasaki A, Matsutani H, Kubota M, Fujimori A, Suzaki K, and Abe Y, "A practical method for estimating high-energy x-ray spectra using the iterative perturbation principle proposed by Waggener," *Radiat. Phys. Chem.* **67**, 81–91 (2003).

[3] Iwasaki A, Kubota M, Hirota J, Fujimori A, Suzaki K, Aoki M, and Abe Y, "Characteristic features of a high-energy x-ray spectra estimation method based on the Waggener iterative perturbation principle," Med. Phys. **33**, 4056-4063 (2006).

[4] Liu HH, Mackie TR, and McCullough EC, "Correcting kernel tilting and hardening in convolution/superposition dose calculations for clinical divergent and polychromatic photon beams," *Med. Phys.* **24**, 1729-1741 (1997).

[5] Ahnesjö A and Aspradakis MM, "Dose calculations for external photon beams in radiotherapy,"*Phys. Med. Biol.* **44**, R99-R155 (1999).

[6] Mackie TR, Scrimger JW, and Battista JJ, "A convolution method of calculating dose for 15-MV x rays," *Med. Phys.* **12**, 188-196 (1985).

[7] Mohan R, Chui C, and Lidofsky L, "Differential pencil beam dose computation model for photons," *Med. Phys.* **13**, 64-73 (1986).

[8] Mackie TR, Bielajew AF, Rogers DWO, and Battista JJ, "Generation of photon energy deposition kernels using the EGS Monte Carlo code," *Phys. Med. Biol.* 33, 1-20 (1988).

[9] Ahnesjö A, "Collapsed cone convolution of radiant energy for photon dose calculation in heterogeneous media," *Med. Phys.* **16**, 577-592 (1989).

[10] Iwasaki A, "A convolution method for calculating 10-MV x-ray primary and scatter dose including electron contamination dose," Med. Phys. **19**, 907-915 (1992).

[11] Iwasaki A, "10 MV X-ray central-axis dose calculation in thorax-like phantoms (water/cork) using the differential primary and scatter method," Radiat. Phys. Chem. **65**, 11-26 (2002).

[12] Iwasaki A, "Comments on the primary and scatter dose-spread kernels used for convolution methods," *Radiat. Phys. Chem.* **65**, 595-597 (2002).

[13] Zhu TC and Bjärngard BE, "Head scatter off-axis for megavoltage x rays," *Med. Phys.* **30**, 533-543 (2003).

Monte Carlo simulation for constructing dose kernels based on the differential dose concept

M Sasamori*[1], A Iwasaki[1], S Hidetoshi[2], S Kimura[1], M Seino[1], F Komai[1]
(1) Hirosaki University, Hirosaki, Aomori, JP
(2) Tokyo Metropolitan University, Arakawa-ku, Tokyo, JP

Purpose: The in-water dose kernels used for convolution methods are usually produced by Monte Carlo simulation with the interaction point forced to the center of a large water phantom. However, it is still not clear whether such Monte Carlo based dose kernels allow accurate dose calculations with a wide range of field sizes and depths, especially in thorax phantoms. Using the differential dose concept, it has been theoretically proved that there is another type of in-water dose kernel, with which perfectly accurate dose calculations can be performed under conditions that the beam is parallel, the incident beam intensity is uniform within and zero outside the field, and the primary beam attenuation coefficient along raylines is not a function of depth and off-axis distance. The in-water dose kernel is a mosaic kernel because it is reconstructed using a set of semi-infinite water phantoms. **Methods and Results:** Using Monte Carlo simulations for a monochromatic 10 MeV photon pencil beam irradiation, we constructed two types of in-water dose kernels: one was an ordinary dose kernel constructed using an infinite water phantom and the other was a mosaic dose kernel reconstructed using a set of semi-infinite water phantoms. Using a convolution method, we calculated two sets of central-axis depth doses in water using the two dose kernels for parallel 10-MeV photon beam irradiations with field radii of 0.1-5 cm. On the other hand, using a Monte Carlo simulation for the same irradiations, we also calculated sets of central-axis depth doses in water. The fact has been obtained that the mosaic dose kernel can generally perform more accurate dose calculations than the ordinary dose kernel, especially when using such small field radii as 0.1 or 0.2 cm.

NOTES:

Introduction

Photon beam dose calculation algorithms in radiotherapy treatment planning systems are slowly changing, with a shift from correction-based methods to model-based approaches such as the convolution or Monte Carlo methods. With respect to the available dosimetry algorithms, only the Monte Carlo method is currently able to account for all aspects of photon and electron transport within homogeneous or heterogeneous media. Monte Carlo simulations represent a powerful tool for studying difficult radiation transport problems such as the effect of tissue heterogeneity and the separation of primary and scatter dose components. However, Monte Carlo techniques are currently too time consuming for conventional radiotherapy treatment planning.

Convolution methods are also able to calculate primary and scatter dose components separately and are convenient for 3-D calculations, especially when using irregular fields and non-uniform incident beams. The technique spatially convolves the primary beam intensity with a dose kernel that describes the transport and energy deposition by secondary particles. The basic dose kernel (or the in-water dose kernel) is usually produced by Monte Carlo simulation with the interaction point forced to the center of a large water phantom [1-5]. However, it is still not clear whether such Monte Carlo based kernels allow accurate dose calculations with a wide range of field sizes and depths, especially in thorax phantoms. Iwasaki [6] has pointed out that the in-water dose kernel should not be yielded with the interaction point forced to the center of a large water phantom, but rather should be yielded using a set of semi-infinite water phantoms on the basis of the differential dose concept [7,8]. In this paper, we will construct these two types of in-water dose kernels using Monte Carlo simulation, and then compare them from the standpoint of convolution-based and Monte Carlo-based depth dose in water.

Theory

This theory is redescribed on referring to Ref. 6. As illustrated in figure 1, we take a semi-infinite water phantom and a parallel photon beam with a circular field with a radius of R. We assume that the incident beam intensity is uniform within and zero outside the field and that the primary beam attenuation coefficient (μ) along raylines is not a function of depth and off-axis distance. For the primary beam intensity to be convolved with a dose kernel, we take the primary water collision kerma [9]. Let K_0 denote an incident water collision kerma, then the primary water collision kerma at a depth Z within the field can be expressed as

$$K(Z) = K_0 \exp(-\mu Z). \tag{1}$$

We set a point O on the beam axis, at which the primary or scatter dose is evaluated. We define $F(Z,R)$ as the primary or scatter dose at the point O, which is at a depth Z for the field radius R. Figure 1 also shows the case of acquiring $F(Z+dZ,R)$ at the point O, which is at a depth $Z+dZ$. Mathematically, we can expand this as

$$F(Z+dZ,R) = F(Z,R) + \partial F(Z,R)/\partial Z dZ. \tag{2}$$

Here we introduce a forward primary or scatter dose kernel function $H_1(Z,r)$, expressing the primary or scatter dose at the point O, arising from a point (Z,r) on the incident surface per unit primary water collision kerma and per unit volume at (Z,r). If the $H_1(Z,r)$ function is taken for the dose calculation, it can be understood that $F(Z+dZ,R)$ is composed of two components when neglecting the primary or scatter dose caused by the interaction between the dZ layer and the phantom yielding $F(Z,R)$. One is the primary or scatter dose produced by the incident primary water collision kerma of $K_0\exp(-\mu dZ)$ for the phantom yielding $F(Z,R)\exp(-\mu dZ)$. The other is the primary or scatter dose arising from the dZ layer. Namely, we have

$$F(Z+dZ,R) = F(Z,R)\exp(-\mu dZ) + 2\pi K_0 dZ \int_0^R H_1(Z,r) r dr. \tag{3}$$

In the equation constructed by letting the right-hand sides of Eqs. (2) and (3) be equal to each other, we make $\exp(-\mu dZ)=1-\mu dZ$ and then differentiate both sides with respect to R, to obtain

$$H_1(Z,R) = [\partial^2 F(Z,R)/\partial Z \partial R + \mu \partial F(Z,R)/\partial R]/(2\pi R K_0). \tag{4}$$

It should be noted that $H_1(Z,R)$ is evaluated for the point situated at the margin of the circular beam field on the phantom surface.

Next, we summarize the forward primary or scatter dose kernel function with a backward primary or scatter dose kernel function. With respect to the two semi-infinite water phantoms illustrated in figure 2, (a) $H_1(\xi,r)$ expresses the forward primary or scatter dose at a point (ξ,r), arising from the pencil-beam interaction point O ($\xi=0,r=0$) situated on the phantom surface, per unit primary water collision kerma per unit volume at point O; and (b) $H_2(\eta,r)$ expresses the backward primary or scatter absorbed dose at a point (η,r) on the phantom surface, arising from the pencil-beam interaction point O ($\eta=0,r=0$) situated at a depth η below the phantom surface, per unit primary water collision kerma per unit volume at point O. With respect to the $H_1(\xi,r)$ and $H_2(\eta,r)$ functions, we can obtain $H_1(0,r)=H_2(0,r)$ for $\xi\to 0$ and $\eta\to 0$.

Using the above $H_1(\xi,r)$ and $H_2(\eta,r)$ functions, we can derive $F(Z,R)$ of figure 1 as

$$F(Z,R)=2\pi K_0\int_0^R\int_0^Z H_1(\xi,r)\exp[-\mu(Z-\xi)]rdrd\xi+2\pi K_0\int_0^R\int_0^r H_2(\eta,r)\exp[-\mu(Z+\eta)]rdrd\eta \qquad (5)$$

The right-hand side of Eq. (5) describes a convolution expression. The first and second terms express the forward and backward dose components, respectively, at the point O. It can also be proved using Eq. (5) itself that the second term is exactly equal to $F(0,R)\exp(-\mu Z)$.

From the above-described theoretical considerations, it may be suggested that for performing more accurate dose calculations, the basic dose kernels (or the in-water dose kernels) used for convolution methods should not be obtained with the interaction point forced to the center of a large water phantom.

The approach employing the $H_1(\xi,r)$ function for scatter dose calculations is essentially the same as the differential scatter method [7,8]. The method of using the $H_1(\xi,r)$ and $H_2(\eta,r)$ functions for calculation of 10 MV x-ray primary and scatter doses has already been developed by Iwasaki [10], where the primary dose kernel is constructed based on the zero-area TMR (tissue-maximum ratio) and the LSD (laterally spread primary dose) function, and the scatter dose kernel is constructed based on the SMR (scatter-maximum ratio).

Monte Carlo simulation

In-water dose kernels and central-axis depth doses in water were simulated using monochromatic E-MeV photons.The EGS4 MC code was used for the simulations. The separation of the primary and the scatter dose was performed using Subroutine AUSGAB. Regarding Monte Carlo-based dose kernels yielded using an infinite or semi-infinite water phantom (refer to figure 2), let $H_1^{MC}(\xi,r)$ denote the forward primary or scatter dose (Gy) at point (ξ,r) per primary photon interaction at point O, and let $H_2^{MC}(\eta,r)$ denote the backward primary or scatter dose (Gy) at point (η,r) per primary photon interaction at point O; therefore, their units are Gy/interaction. Regarding the $H_1(\xi,r)$ and $H_2(\eta,r)$ functions, each of them expresses the primary or scatter dose (Gy) at point (ξ,r) or (η,r) per unit primary water collision kerma (Gy) per unit volume (cm^3) at point O; therefore, their units are cm^{-3}. The relations between $H_1^{MC}(\xi,r)$and $H_1(\xi,r)$ and between $H_2^{MC}(\eta,r)$and $H_2(\eta,r)$ become as follows:

$$H_1(\xi,r)=H_1^{MC}(\xi,r)/K_S \quad (cm^{-3}), \qquad (6)$$

$$H_2(\eta,r)=H_2^{MC}(\eta,r)/K_S \quad (cm^{-3}), \qquad (7)$$

$$K_S=[E\cdot(\mu_{en}(E)/\rho)_{water}/\mu(E)_{water}]\times 1.602\times 10^{-10} \quad (Gy\ cm^3), \qquad (8)$$

where E is the primary photon energy in MeV, $(\mu_{en}(E)/\rho)_{water}$ is the mass energy absorption coefficient (cm^2/g) of water for photon energy E, and $\mu(E)_{water}$ is the linear attenuation coefficient (cm^{-1}) of water for photon energy E. K_S expresses the primary water collision kerma (Gy) to raise one primary photon interaction per unit volume (cm^3) at point O.

Results and summary

Experiments were performed using monochromatic photons of E=10 MeV. The $(\mu_{en}(E)/\rho)_{water}$ and $\mu(E)_{water}$ values were obtained from Hubbell [11]. We constructed two types of in-water dose kernels (Gy/interaction) using Monte Carlo simulations and converted them to in-water dose kernels (cm^{-3}) of Eqs. (6) and (7), where the voxel sizes were 0.5×0.5 mm^2. One was the primary dose kernel (or the ordinary dose kernel) yielded with an interaction point forced to the center of a large water phantom, as shown in figure 3(a) (the dose kernel value at the voxel of the photon interaction point O is 87.6 cm^{-3}). The other was the mosaic primary dose kernel yielded using a set of semi-infinite water phantoms, as shown in figure 3(b) (the dose kernel value at the voxel of the photon interaction point O is 42.5 cm^{-3}). Both primary dose distributions around the photon interaction point O are largely different with each other; however, both primary dose distributions far from the photon interaction point O are almost the same.

Three types of primary dose calculations were performed in water along the central axis for field radii of R=0.1-5 cm, with an incident primary water collision kerma of $K_0=1.131\times10^{-9}$ Gy (refer to figure 1): one was yielded directly based on Monte Carlo simulation, another was yielded using Eq. (5) with the ordinary dose kernel in figure 3(a), and still another was yielded using Eq. (5) with the mosaic dose kernel in figure 3(b). It should be noted that at this stage, the convolution dose calculation was simply performed using the average dose value itself of each voxel. Figure 4 illustrates results for (a) R=0.1 cm, (b) 0.2 cm, (c) R=0.5 cm, and (d) R=5 cm.

From the results in figure 4, it can be seen that the mosaic dose kernel can generally perform more accurate dose calculations than the ordinary dose kernel. The details are as follows:

(a) At the field radii of R=0.5 cm and R=5 cm, both the ordinary and mosaic dose kernels leads to almost the same calculation

results, which are almost the same calculation results as with the Monte Carlo simulation.

(b) At the field radii of R=0.1 cm and R=0.2 cm, the mosaic dose kernel leads to more accurate dose calculations in relatively deep regions than the ordinary dose kernel does, when comparing their calculation results with that due to the Monte Carlo simulation.

(c) At the field radius of R=0.1 cm, the mosaic dose kernel leads to dose calculation results slightly different from those due to the Monte Carlo simulation. There are also cases in which at shallow depths, the mosaic dose kernel leads to dose calculation results slightly different from those due to the Monte Carlo simulation. These facts may be caused by the convolution dose calculation technique of simply using the average dose value itself for each voxel.

(d) There are cases in which at shallow depths, the mosaic dose kernel leads to dose calculation results somewhat different from those due to the Monte Carlo simulation.

Therefore, it can be understood that the mosaic dose kernel may lead to more accurate dose calculation results in thorax phantoms when using small fields (however, it is still not confirmed experimentally). This paper performs convolution dose calculations only using monochromatic 10 MeV photons. In the future, we will study using other monochromatic photons and x-ray beams composed of multiple spectral energy bins. The idea of using very small fields of R<0.5 cm may be useful for evaluation criteria of dose calculations due to the MLC interleaf x-ray transmission and for evaluation criteria of convolution dose calculations especially for IMRT (intensity modulated radiation therapy).

References

[1] Mackie TR, Scrimger JW, and Battista JJ, "A convolution method of calculating dose for 15-MV X-rays," *Med. Phys.* **12**, 188–196 (1985).

[2] Mohan R, Chui C, and Lidofsky L, "Differential pencil beam dose computation model for photons," *Med. Phys.* **13**, 64–73 (1986).

[3] Ahnesjö A, Andreo P, and Brahme A, "Calculation and application of point spread functions for treatment planning with high energy photon beams," *Acta Oncol.* **26**, 49–56 (1987).

[4] Mackie TR, Bielajew AF, Rogers DWO, and Battista JJ, "Generation of photon energy deposition kernels using the EGS Monte Carlo code, " *Phys. Med. Biol.* **33**, 1–20 (1988).

[5] Ahnesjö A, "Collapsed cone convolution of radiant energy for photon dose calculation in heterogeneous media," *Med. Phys.* **16**, 577–592 (1989).

[6] Iwasaki A, "Comments on the primary and scatter dose-spread kernels used for convolution methods," *Radiat. Phys. Chem.* **65**, 595-597 (2002).

[7] Cunningham JR, "Scatter-air ratios," *Phys. Med. Biol.* **17**, 42–51 (1972).

[8] Iwasaki A, Ishito T, "The differential scatter-air ratio and differential backscatter factor method combined with the density scaling theorem," *Med. Phys.* **11**, 755–763 (1984).

[9] Attix FH, *Introduction to Radiological Physics and Radiation Dosimetry*, (Wiley-Interscience, New York, 1986), pp. 24–26.

[10] Iwasaki A, "A convolution method for calculating 10-MV x-ray primary and scatter dose including electron contamination dose," *Med. Phys.* **19**, 907–915 (1992).

[11] Hubbell JH, "Photon mass attenuation and energy-absorption coefficients from 1 keV to 20 MeV," *Int. J. Appl. Radiat. Isot.* **33**, 1269-1290 (1982).

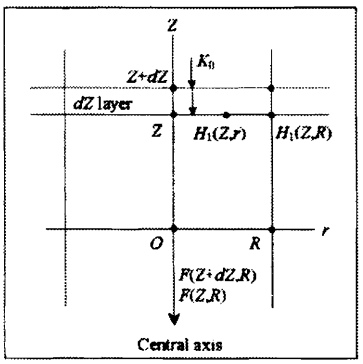

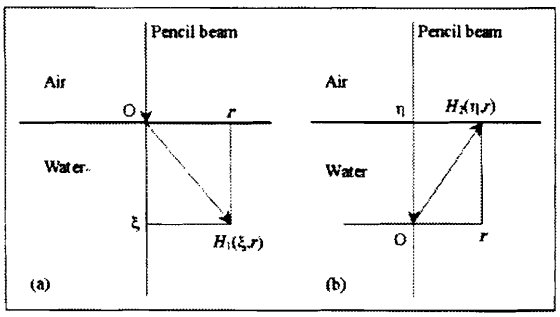

Figure 1. Using a semi-infinite water phantom, $F(Z,R)$ and $F(Z+dZ,r)$ are defined as the primary or scatter absorbed doses at the point O at depths Z and $Z+dZ$, respectively, on the beam axis for a parallel photon beam irradiation with a field radius of R and an incident water collision kerma of K_0.

Figure 2. Diagrams showing how (a) the $H_1(\xi,r)$ function and (b) the $H_2(\eta,r)$ function should be used in water for a given pencil beam, where the interaction point is situated at point O.

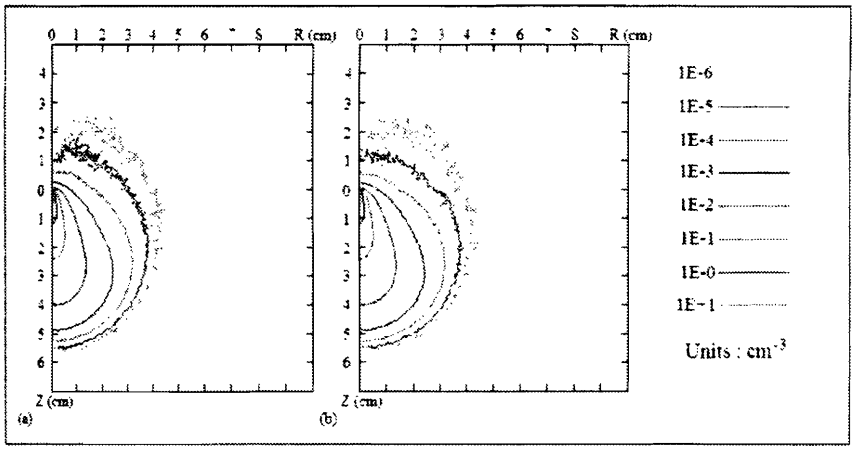

Figure 3. (a) An ordinary primary dose kernel and (b) a mosaic primary dose kernel for photon energy of 10 MeV.

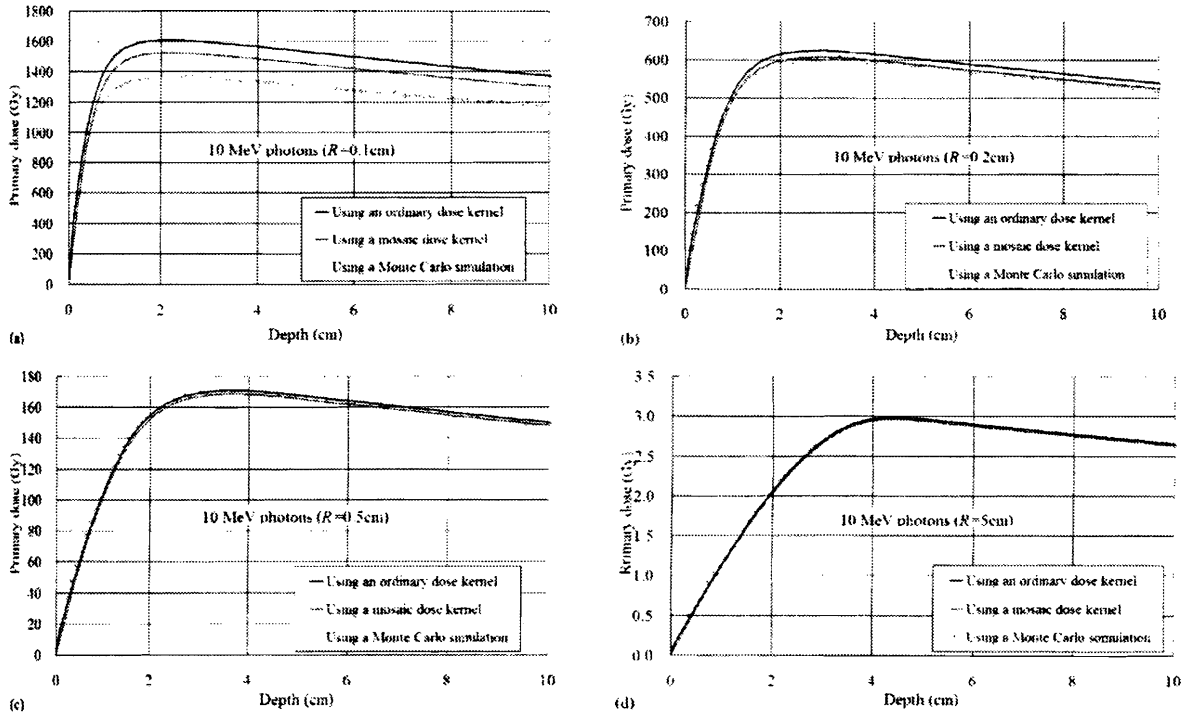

Figure 4. Three types of central-axis primary dose data in water for field radii of (a) R=0.1 cm, (b) R=0.2 cm, (c) R=0.5 cm, and (d) R=5 cm, with an incident primary water collision kerma of $K_0=1.131\times10^{-9}$ Gy (figure 1): One was yielded using an ordinary dose kernel (figure 3(a)), another yielded using a mosaic dose kernel (figure 3(b)), and still another yielded directly based on Monte Carlo simulation.